Electronic Supplementary Material (ESI) for Journal of Materials Chemistry A.
This journal is © The Royal Society of Chemistry 2020

Supporting Information

Ultrastable Lithium-Sulfur Batteries with Outstanding Rate Capability Boosted by NiAs-Type Vanadium Sulfides

Chao Yue Zhang,[a] Guo Wen Sun,[a] Yun Fei Bai, [b] Zhe Dai,[a] Yi Rong Zhao,[a] Xiu Ping Gao, [a] Geng Zhi Sun,[c,d] Xiao Bo Pan, [b] Xiao Jun Pan*[a] and Jin Yuan Zhou*[a]

[a.] Key Laboratory for Special Function Materials & Structural Design of the Ministry of Education, and School of Physical Science & Technology, Lanzhou University, 222 South Tianshui Road, Lanzhou 730000, China

[b.] State Key Laboratory of Applied Organic Chemistry, College of Chemistry and Chemical Engineering, Key Laboratory of Nonferrous Metal Chemistry and Resources Utilization of Gansu Province, Lanzhou University, Lanzhou, 730000, China

[c.] Key Laboratory of Flexible Electronics & Institute of Adv. Mater., Nanjing Tech University, 30 South Puzhu Road, Nanjing 211816, China

[d.] School of Material Science and Engineering, Henan Polytechnic University, 2001 Shiji Road, Jiaozuo 454003, China

XRD patterns

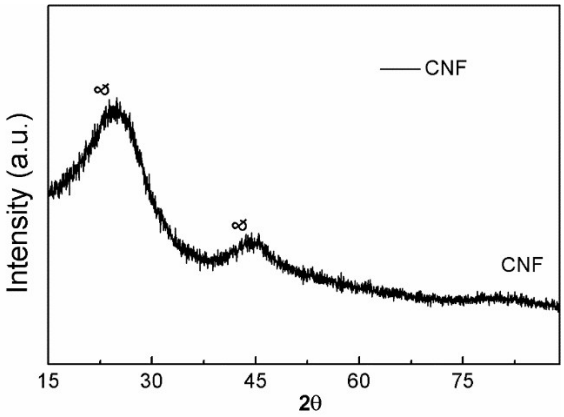

Figure S1 XRD patterns curve of the CNF.

SEM images

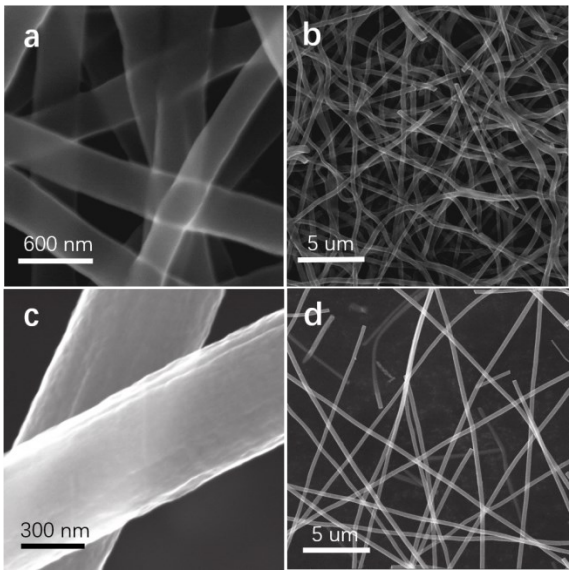

Figure S2 High and low-resolution SEM images of CNF and CNF@$VO_{0.9}$.

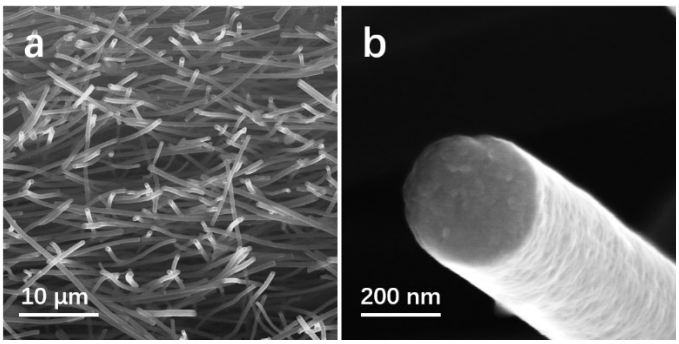

Figure S3. (a) SEM image of cut V_2S_3 nanofibers, and (b) cross-section view SEM image of a CNF@ V_2S_3 composite nanofiber.

Raman pattern

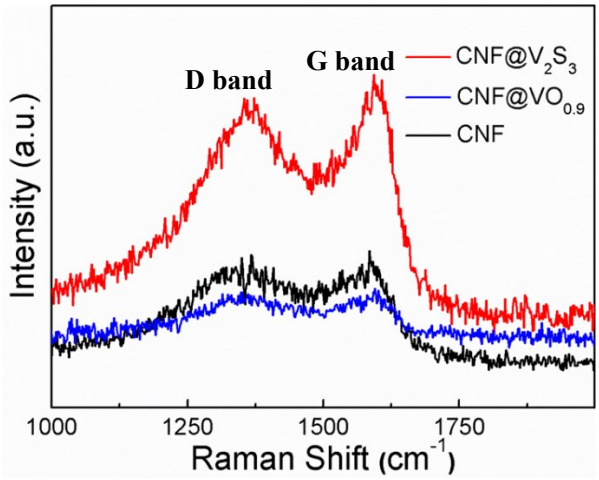

Figure S4 Raman spectrum of CNF@V_2S_3, CNF@$VO_{0.9}$ and CNF.

XPS spectra of O 1s cores

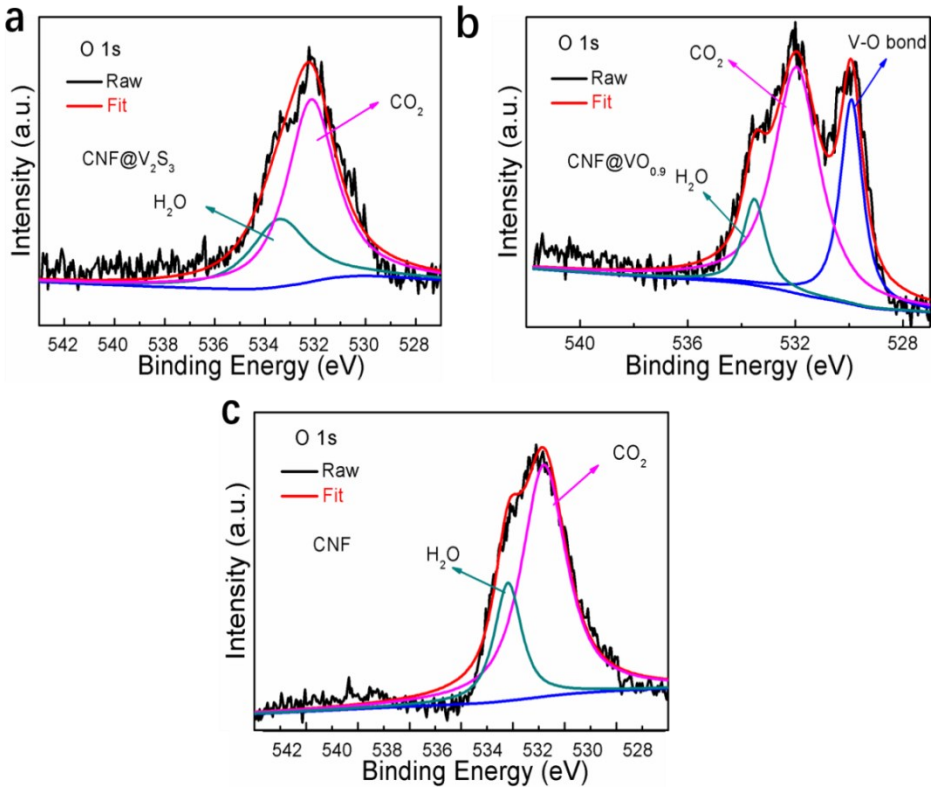

Figure S5 O elemental signal image of XPS of CNF@V_2S_3 (a) CNF@$VO_{0.9}$ (b) and CNF (c).

To make clear the origin of oxygen, the high-resolution O 1s XPS spectra of CNF@V_2S_3, CNF@$VO_{0.9}$ and pure CNFs have been studied together. As presented in

Figure S4, the O 1s XPS peak of CNF@V_2S_3 are similar with that of the pure CNFs, and can be decomposed into two components, located at 533.5 and 532.0 eV, respectively; while the O 1s XPS peak of CNF@$VO_{0.9}$ can be decomposed into three components, located at 533.5, 532.0, and 529.9 eV, respectively. The peak at 529.9 eV corresponds to the V-O bonds, the peaks at 533.5 and 532.0 eV are often caused by the adsorbed H_2O and CO_2 molecules in air, respectively.[1]

Optical photos

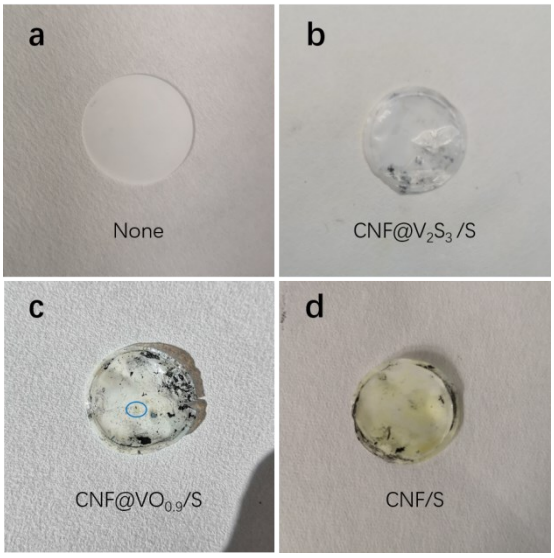

Figure S6 Photos of battery separator (a), the cycled battery separators of CNF@V_2S_3/S(b), CNF@$VO_{0.9}$/S(c) and CNF/S (d).

TGA data

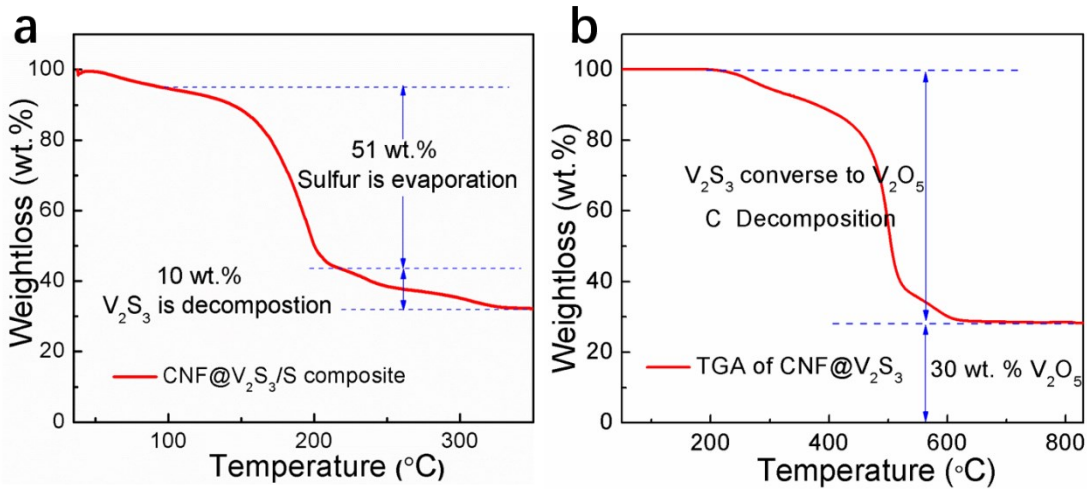

Figure S7 (a) The TGA curve of CNF@V_2S_3/S composite electrode. (b) The TGA curve of CNF@V_2S_3 electrode in air.

For the analysis of TGA curve of CNF@V_2S_3 electrode in air as shown in Figure S7b, the final phase after calcination is V_2O_5, therefore, the V_2O_5 content is about 30 wt.%. According to V element mass balance (Formula 1), the V_2S_3 content is 32.7 wt.%, and the content of the carbon is about 67.3 wt%.

$$V_2S_3 + O_2 \rightarrow V_2O_5 \qquad [1]$$

Cross-section SEM image

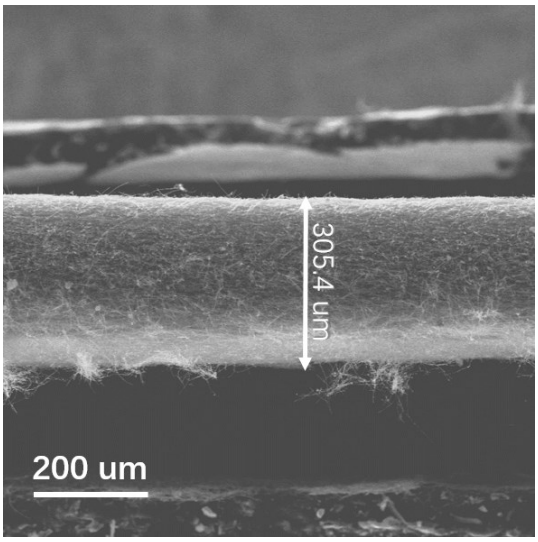

Figure S8 Thickness of CNF@V_2S_3 electrode

CV analysis

Table S1. Positions of reduction peaks in the CV curves. [2-6]

	First reduction peak (V)	Second reduction peak (V)	D-value (mV)
CNF@V_2S_3/S	**2.054**	**2.325**	**271**
CNF@$VO_{0.9}$/S	**2.029**	**2.307**	**278**
CNF/S	**2.026**	**2.308**	**282**
Ref.2	**2.03**	**2.31**	**280**
Ref.3	**2.04**	**2.31**	**270**
Ref.4	**2.01**	**2.33**	**320**
Ref.5	**2.01**	**2.29**	**280**
Ref.6	**1.95**	**2.25**	**300**

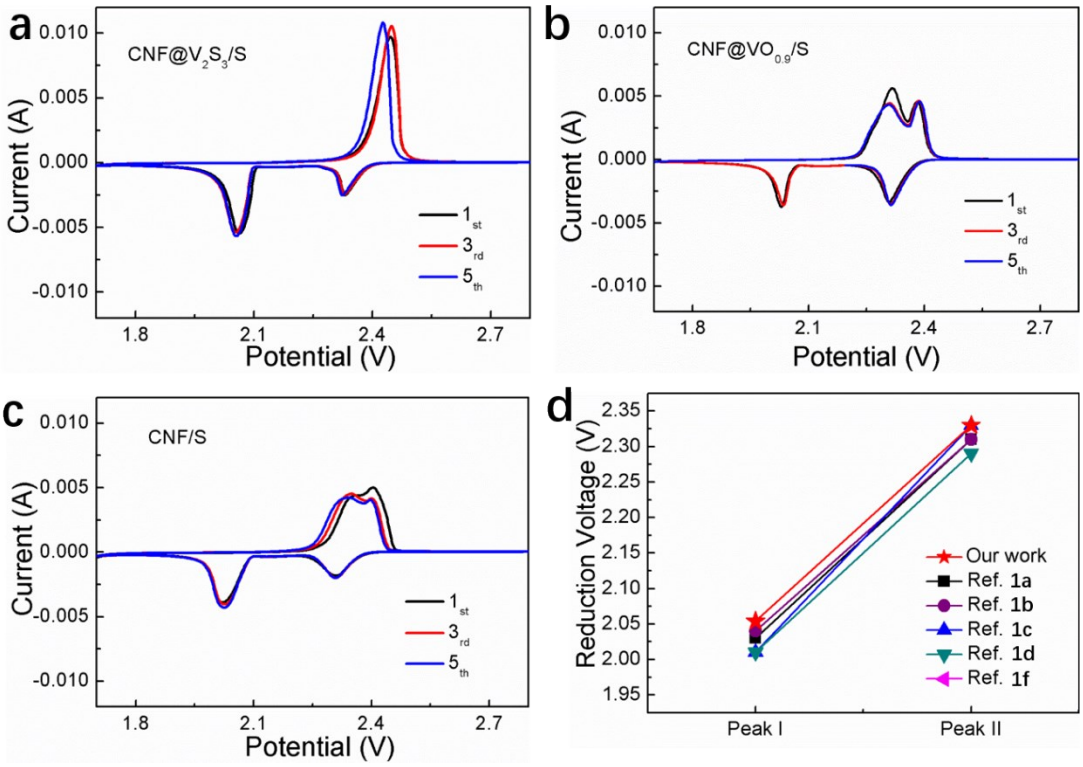

Figure S9 The initial five cycles of CV curves for (a) CNF@V_2S_3/S, (b) CNF@$VO_{0.9}$/S and (c) CNF/S. The Vanadium-based LSB comparison of the reduction peak position (d) in the recent literature [2-6]

Electrochemical performance of host

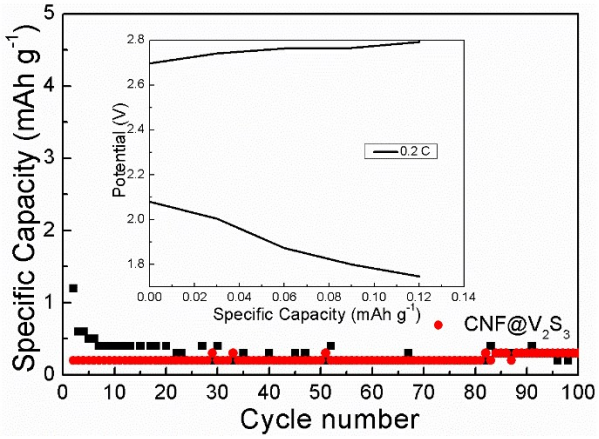

Figure S10 The electrochemical performance of CNF@V_2S_3 based compounds without sulfur.

Capacity contribution ratios

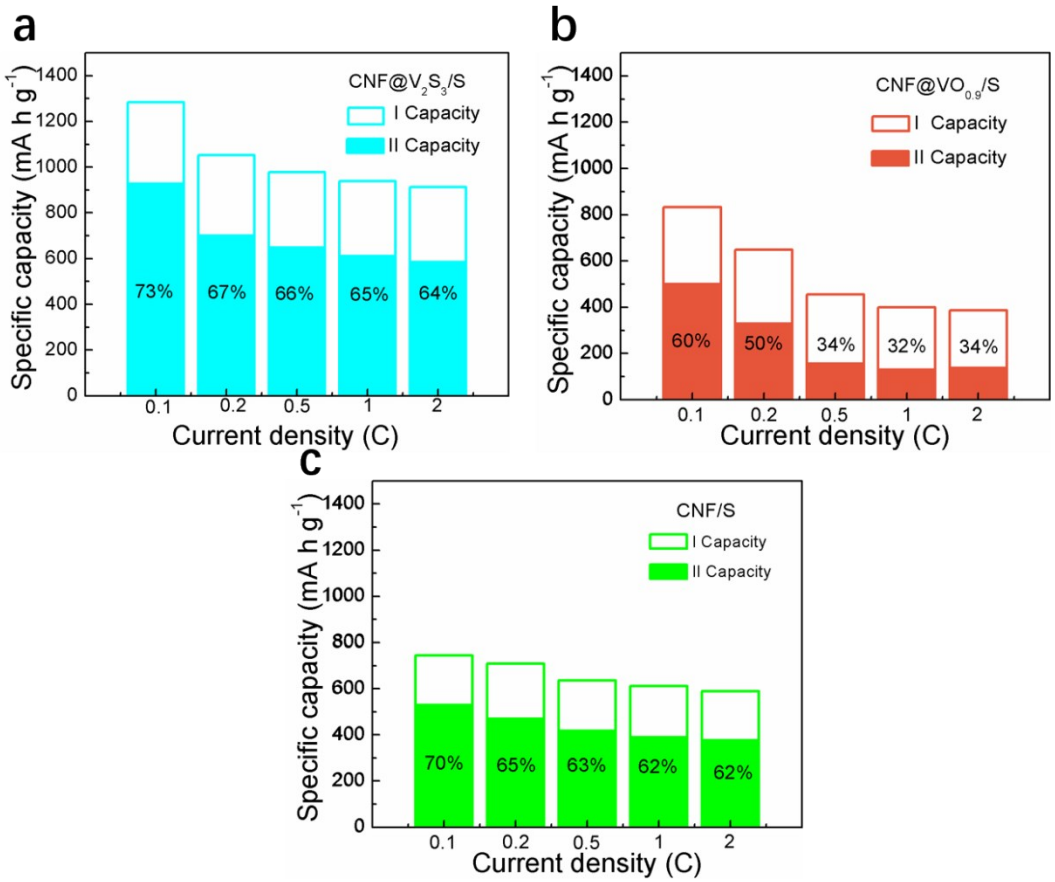

Figure S11 Capacity contributions of soluble Li_2S_4, Li_2S_6 and Li_2S_8 conversion (I) and insoluble Li_2S_2/Li_2S conversion (II) and the corresponding capacity ratios (II/I) at different rates for the (a) CNF@V_2S_3 , (b) CNF@$VO_{0.9}$/S and (c) CNF/S cathodes.

Due to the relatively slow reaction kinetics of intermediate LiPSs, it is difficult to convert them into the final reduction products Li_2S/Li_2S_2 completely during the reduction II, often resulting into an II/I ratio less than 3. Thus, the closer the ratio is to 3, the higher the reversible specific capacity is.

Calculation of reduction resistance

The calculation way of in situ reaction resistance: The difference between quasi-open-circuit potential and closed-circuit potential is used to calculate the over-potentials, and then the in-situ reaction resistance can be calculated as,[7]

$$R = \frac{\Delta U}{m \times J}, \qquad [2]$$

where, ΔU is the over-potential, m is the mass loading of sulfur, and J is the charge/discharge current density.

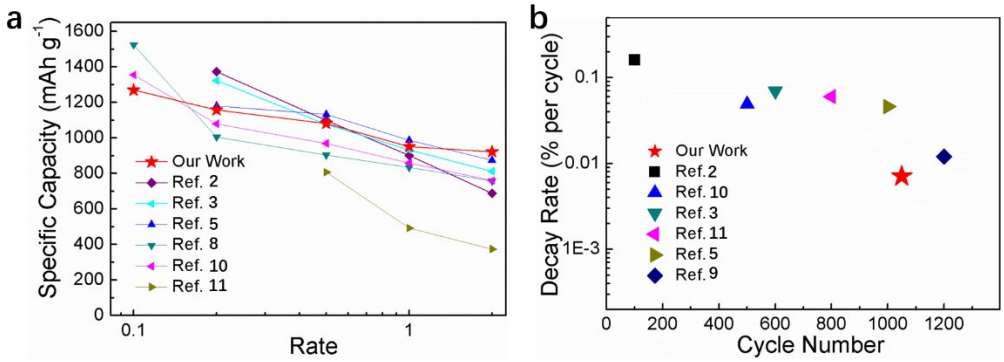

Figure S12 Long cycle comparison of the rate capabilities (a) and decay rate (b) of CNF@V_2S_3/S in the recent literature.[2, 3, 5, 8-11]

Quasi in-situ SEM image

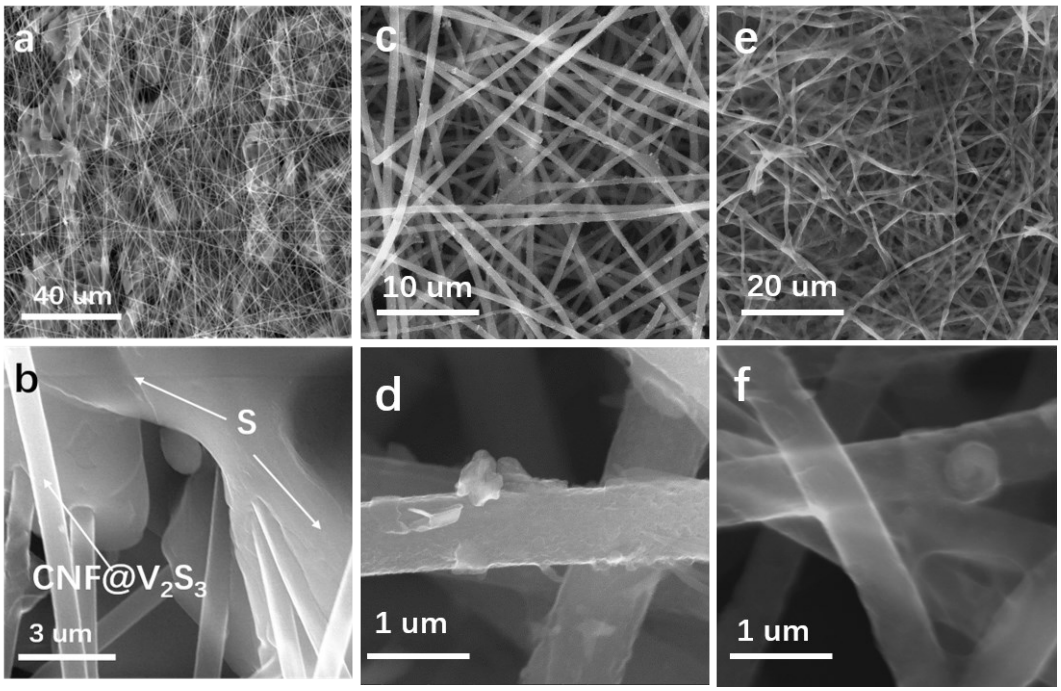

Figure S13 SEM images of the CNF@V_2S_3/S cathodes: (a-b) before cycling, (c-d) after 100 cycles at 2 C, and (e-f) after 1000 cycles at 2 C, respectively.

EIS spectra

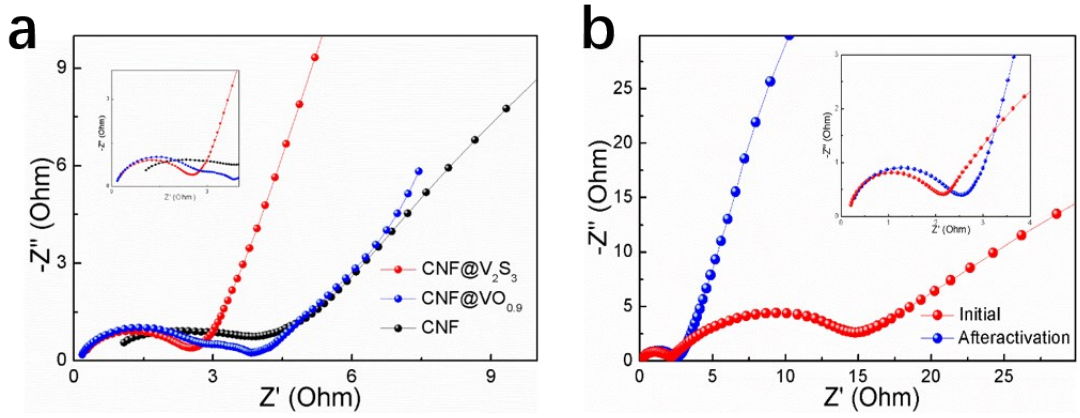

Figure S14 (a) The EIS curves of CNF@V_2S_3/S, CNF@$VO_{0.9}$/S and CNF/S. Inset: the magnified high frequency region. (b) Nyquist plots of the CNF@V_2S_3/S composites electrode before activation and after activation. Inset: the magnified high frequency region.

Table S2. Corresponding fitting result of *Rs* and *Rct* values for the Nyquist plots.

	R_s	R_{ct}	Slope of low frequency region
CNF@V_2S_3/S	**0.27**	**2.63**	**1.46**
CNF@$VO_{0.9}$/S	**0.28**	**3.82**	**0.97**
CNF/S	**1.10**	**3.97**	**0.62**

Table S3. Corresponding CNF@V_2S_3/S result of *Rs* and *Rct* values for the Nyquist plots.

	R_s	R_{ct}	Slope of low frequency region
OCV	**0.28**	**15.2**	**0.83**
After activation	**0.27**	**2.63**	**1.46**

The obtained Nyquist plots were semicircular at the high frequency section and increases sharply at the low frequency section. In the high band, the real left intersection (-Z'') is related to the series resistance (R_s).[12] The semi-circular region in the plots corresponds to the charge transfer resistance (R_{ct}), indicting the interface resistance of the electrolyte and the electrode surface. In the low frequency region, the greater the slope of the curve, the greater the diffusion rate of the Li ions in the electrolyte, even the proximity of 90° may ignore the diffusion resistance.[12]

EIS spectra shown in Fig. S12 indicates that compared to CNF@$VO_{0.9}$/S and CNF/S cathodes, the CNF@V_2S_3/S ones show a smaller series resistance (R_s) and a charge transfer resistance (R_{ct}),[12] again indicating an enhanced electron/ion kinetics.[13] And, the curve slope in the low-frequency region of CNF@V_2S_3/S cathodes is much larger than those of CNF@$VO_{0.9}$/S and CNF/S ones, further implying a higher diffusivity of electrolyte ions in CNF@V_2S_3/S cathodes.

GITT analysis

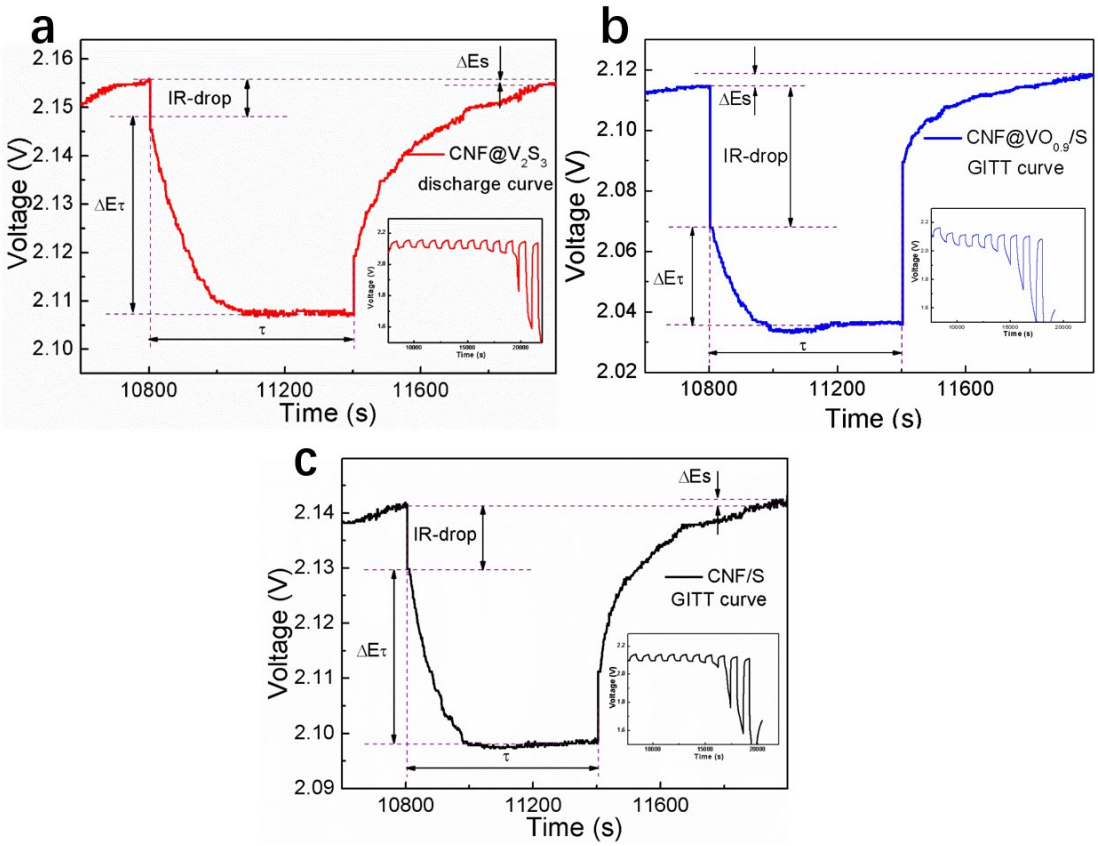

Figure S15 (a-c) GITT potential response curve with time for one typical discharge step of CNF@V_2S_3/S, CNF@$VO_{0.9}$/S and CNF/S. Inset: GITT profiles of the discharging process selected rest discharge-rest period.

GITT measurement was performed by a current density at 0.2 C for 10 min and rest intervals for 10 min. The Fick's second law using the equation estimated the Li^+ diffusion coefficients in CNF@V_2S_3/S electrode:[14, 15]

$$D_{Li^+} = \frac{4}{\pi\tau}\left(\frac{m_B V_m}{M_B S}\right)^2\left(\frac{\Delta E_s}{\tau\left(dE_\tau/d\sqrt{\tau}\right)}\right)^2, \quad [3]$$

If the potential *vs.* $\tau_{1/2}$ (τ is pulse current duration time) displays a linear behavior, equation diffusion can be further simplified as below:

$$D_{Li^+} = \frac{4}{\pi\tau}\left(\frac{m_B V_m}{M_B S}\right)^2\left(\frac{\Delta E_s}{\Delta E_\tau}\right)^2, \quad [4]$$

Table S4 Li-ion diffusion rates between cathode and electrolyte

Samples	Second reduction peak (cm^2 s^{-1})
CNF@V_2S_3/S	2.857×10^{-6}
CNF@$VO_{0.9}$/S	1.554×10^{-7}
CNF/S	1.645×10^{-7}

Optical photo

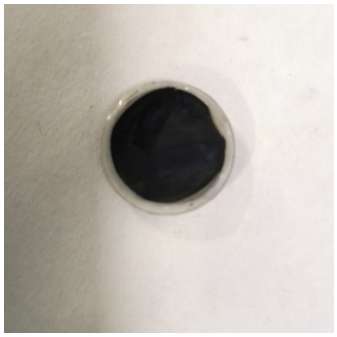

Figure S16 the Optical photo of CNF@V_2S_3/S cathode after 500 cycles.

Catalytic performance

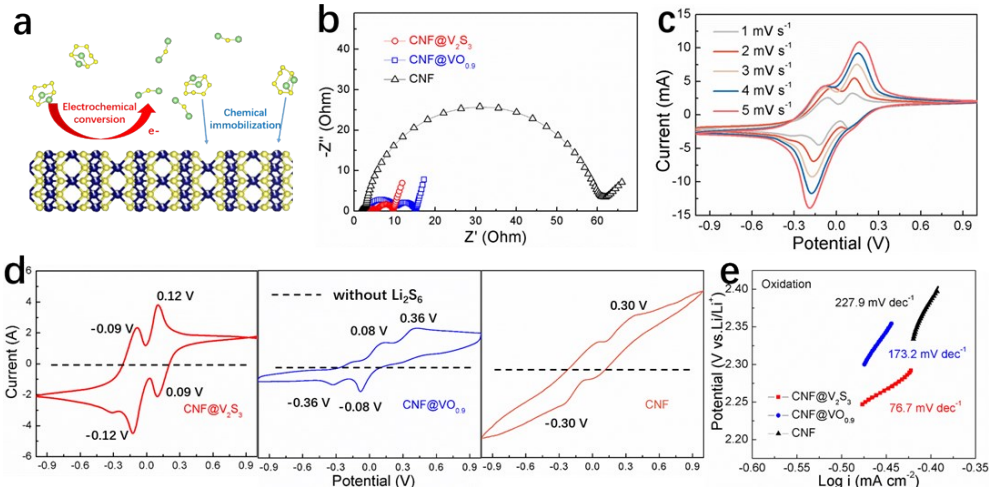

Figure S17. a) Schematic illustration of the LiPSs' conversion on the surface of V_2S_3; b) EIS spectra of CNF@V_2S_3, CNF@$VO_{0.9}$ and CNF cells without sulfur addition. c) CV profiles of CNF@V_2S_3 cells under different scan rates. d) CV curves of CNF@V_2S_3, CNF@$VO_{0.9}$ and CNF cells at 1 mV s^{-1}; e) Tafel plots of Li_2S oxidization on CNF@V_2S_3, CNF@$VO_{0.9}$ and CNF electrodes.

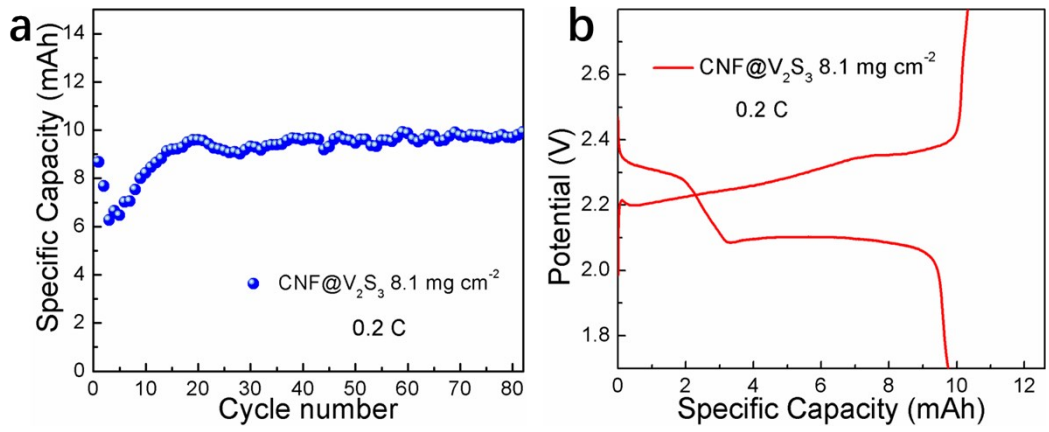

Figure S18. The sulfur high loading of CNF@V_2S_3/S electrode up to 8.1 mg cm^{-2}: (a) cycle performance; (b) charge and discharge profiles.

Self-discharge formula

We define the self-discharge rate as the ratio of lost discharge capacity to initial capacity:

$$Self-discharge\ rate = \frac{C_{ini} - C_{fin}}{C_{ini}} \times 100\% \quad , \qquad [5]$$

where C_{ini} is the initial discharge capacity and C_{fin} is the retention capacity.[16]

1. J. M. S. C. MORANT, L. GALAN, L. SORIANO, F. RUEDA, *Sur.Sci.*, 1989, **218**, 311-345.
2. X. Zhu, W. Zhao, Y. Song, Q. Li, F. Ding, J. Sun, L. Zhang and Z. Liu, *Adv. Energy Mater.*, 2018, **8**, 1800201.
3. Z. X. Cheng, Zhubing Pan, Hui Wang, Shiqing Wang, Ruihu, *Adv. Energy Mater.*, 2017, **8**, 1702337.
4. T. Guo, Y. Song, Z. Sun, Y. Wu, Y. Xia, Y. Li, J. Sun, K. Jiang, S. Dou and J. Sun, *J. Energy Chem.*, 2020, **42**, 34-42.
5. H. Wu, Y. Huan, D. Wang, M. Li, X. Cheng, Z. Bai, P. Wu, W. Peng, R. Zhang, Z. Ji, M. Zou and X. Yan, *J. Electrochem. Soc.*, 2019, **166**, A188-A194.
6. X. Chen, G. Du, M. Zhang, A. Kalam, S. Ding, Q. Su, B. Xu and A. G. Al-Sehemi, *Energy*

Technol., 2019, **8**.

7. T. Liu, S. Sun, W. Song, X. Sun, Q. Niu, H. Liu, T. Ohsaka and J. Wu, *J. Mater. Chem. A*, 2018, **6**, 23486-23494.
8. Y. Song, W. Zhao, N. Wei, L. Zhang, F. Ding, Z. Liu and J. Sun, *Nano Energy*, 2018, **53**, 432-439.
9. Y. Zhang, G. Xu, Q. Kang, L. Zhan, W. Tang, Y. Yu, K. Shen, H. Wang, X. Chu, J. Wang, S. Zhao, Y. Wang, L. Ling and S. Yang, *J. Mater. Chem. A*, 2019, **7**, 16812-16820.
10. R. Carter, L. Oakes, N. Muralidharan, A. P. Cohn, A. Douglas and C. L. Pint, *ACS Appl. Mater. Interfaces*, 2017, **9**, 7185-7192.
11. J. Wei, H. Su, C. Qin, B. Chen, H. Zhang and J. Wang, *J. Electroanal. Chem.*, 2019, **837**, 184-190.
12. C. Yang, X. Ou, X. Xiong, F. Zheng, R. Hu, Y. Chen, M. Liu and K. Huang, *Energy Environ. Sci.*, 2017, **10**, 107-113.
13. X. Yang and A. L. Rogach, *Adv. Energy Mater.*, 2019, **9**, 1900747.
14. C. Bommier, T. W. Surta, M. Dolgos and X. Ji, *Nano Lett.*, 2015, **15**, 5888-5892.
15. Z. Jian, Z. Xing, C. Bommier, Z. Li and X. Ji, *Adv. Energy Mater.*, 2016, **6**.
16. H. S. Ryu, H. J. Ahn, K. W. Kim, J. H. Ahn, K. K. Cho and T. H. Nam, *Electrochim. Acta*, 2006, **52**, 1563-1566.